pp 416–432. © Royal Aeronautical Society 2019
doi:10.1017/aer.2018.167

On-ground lateral direction control for an unswept flying-wing UAV

Z. Y. Ma
School of Astronautics
Science and Technology on UAV Laboratory
Northwestern Polytechnical University
Xi'an
China

X. P. Zhu
Science and Technology on UAV Laboratory
Northwestern Polytechnical University
Xi'an
China

Z. Zhou
zhouzhou@nwpu.edu.cn
School of Aeronautics
Northwestern Polytechnical University
Xi'an
China

ABSTRACT

To solve the on-ground lateral direction control problem of the unswept flying-wing unmanned aerial vehicle (UAV) without rudder, steering system or breaking system, a control approach which uses differential propeller thrust to control the lateral direction is proposed. First, a mathematical model of the unswept flying-wing UAV on-ground moving is established. Second, based on the active disturbance rejection control (ADRC) theory, a yaw angle controller is designed by using the differential propeller thrust as the control output. Finally, a straight line trajectory tracking control law is designed by improving the vector field path following method.

Received 21 May 2018; revised 17 November 2018; accepted 21 November 2018.

https://doi.org/10.1017/aer.2018.167 Published online by Cambridge University Press

Experiment results show that the proposed control laws have a shorter response time, better robustness and better control precision compared with proportional integral derivative (PID) controller. The proposed controller has small computational complexity, simple parameter setting process, and uses practical measurable physical quantities, providing a reference solution for further engineering applications.

Keywords: Unswept flying-wing unmanned aerial vehicle; On-ground control; Active disturbance rejection control; Vector field path following; Differential propeller thrust

NOMENCLATURE

F_n, F_f, F_s	vertical force, frictional force and side force on tires
H	the distance between aircraft centre of gravity to ground
h	the distance between aircraft centre of gravity to ground when the tires are not compressed
a_f, a_r	horizontal distance from front tires and rear tires to the center of gravity
b_t	distance between the tires and the symmetric plane of the UAV
d_p	distance between the propellers and the symmetric plane of the UAV
$\boldsymbol{F}_{b_t}, \boldsymbol{F}_{b_p}, \boldsymbol{F}_{b_a}, \boldsymbol{F}_{b_g}$	ground force, propeller thrust, aerodynamic force and gravity
$\boldsymbol{M}_{b_t}, \boldsymbol{M}_{b_p}, \boldsymbol{M}_{b_a}$	ground moment, propeller thrust moment and aerodynamic moment
S_p, C_p, V_p	disk area, thrust coefficient and inflow speed of the propeller
V_{pl}, V_{pr}	inflow speed of the left and right propeller
F_p, ΔF_p	the thrust of propeller and the differential propeller thrust
F_{pl}, F_{pr}	the thrust of left and right propeller
DCM_{bw}, DCM_{be}	direction cosine matrix from wind axes to body-fixed axes and from earth axes to body-fixed axes
m, g	mass of the aircraft, gravity acceleration
S, b, c	the reference area, wing span and mean aerodynamic chord
P_n, P_e, P_d	inertial north, east and down position of the UAV
u, v, w	body frame velocities
p, q, r	roll, pitch and yaw angular rates
V_a, V	airspeed, ground speed
F_L, F_Y, F_D	aerodynamic lift, lateral and drag forces
C_L, C_Y, C_D	aerodynamic lift, lateral and drag forces coefficient
M_l, M_m, M_n	aerodynamic roll, pitch and yaw moments
C_l, C_m, C_n	aerodynamic roll, pitch and yaw moments coefficient
$C_{Y_p}, C_{l_p}, C_{n_p}$	aerodynamic lateral force, roll and yaw moments derivatives with respect to p
$C_{L_q}, C_{D_q}, C_{m_q}$	aerodynamic lift, drag and pitch moment derivatives with respect to q
$C_{Y_r}, C_{l_r}, C_{n_r}$	aerodynamic lateral force, roll and yaw moments derivatives with respect to r
J	inertia tensor
J_{xx}, J_{yy}, J_{zz}, J_{xz}	moments of inertia and product of inertia
d	the lateral distance of the UAV from the straight line path
$V_{\min}$	the lowest speed used in controllers

https://doi.org/10.1017/aer.2018.167 Published online by Cambridge University Press

Greek symbol

α, β	angle of attack and sideslip
δ_t, $\dot{\delta}_t$	compression and compression speed of tires
k_{δ_t}, c_{δ_t}	equivalent stiffness and equivalent damping coefficient of tires
μf, ks, βs	frictional coefficient, cornering stiffness and slip angle of tires
ρ	air density
φ, θ, ψ	roll, pitch and yaw angulars
δp, $\Delta\delta p$	throttle and differential throttle
ψt	the direction angle of the straight line path
$\psi\infty$	the maximum value of the angle between ψc and ψt

1.0 INTRODUCTION

The unswept flying-wing has a high aspect ratio wing with constant chord. Compared with the conventional configuration, this kind of configuration has higher aerodynamic efficiency and more concise structure, which is usually used in solar-powered unmanned aerial vehicle (UAV), such as Pathfinder[1, 2] and Helios[3, 4]. The unswept flying-wing usually consists of a central wing, two outer wings, two vertical stabilisers and a pair of landing gears, as shown in Fig. 1. Because the on-ground moving only accounts for a small proportion of the whole flight process, the landing gear is designed extremely simple in order to reduce weight. The landing gear only consists of four wheels and two supports without front wheel steering system, shock absorbing system or breaking system. Meanwhile, the unswept flying-wing does not have rudder, thus the differential propeller thrust is the only way to control the lateral direction in the process of on-ground moving. Ground forces and moments dominate when the aircraft is running on-ground at low speed. When the aircraft goes faster, the aerodynamic forces and moments must be taken into consideration. Because the movement of UAV on the ground is affected by the environment which is not easy to measure, such as ground types, gusts and small obstacles, the robustness of the controller is highly demanded.

To design an effective control law, a comprehensive understanding of the dynamic model is essential. For most conventional UAVs which have three wheels and front wheel steering system, their on-ground moving models and controllers have been reported in literatures. Zhang[5] established a non-linear model of the UAV during takeoff and designed the take-off control law based on gain scheduling approach. The nose wheel steering, differential brake and rudder were used in control law as controller outputs at different speeds. Lemay[6] also proposed yaw controller using gain scheduling approach to manoeuvre the aircraft on ground. Chen[7] designed an aircraft-on-ground path following control law based on dynamical adaptive back-stepping method, while Fabrizio[8] developed a control system for an aircraft taxiing on ground based on sliding mode feedback control theory and feedforward control theory. Biannic[9] got the aircraft-on-ground model by using the linear fractional transformation method. In order to simplify the mathematical model, the previous papers only

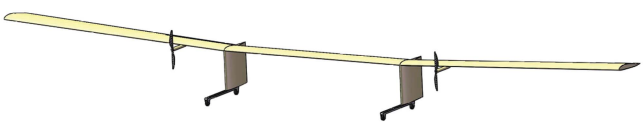


Figure 1. The unswept flying-wing configuration.

https://doi.org/10.1017/aer.2018.167 Published online by Cambridge University Press

consider the lateral dynamics of the vehicle but the roll and pitch dynamics are neglected. Meanwhile, most papers have designed the on-ground controllers by using the front wheel steering and rudder deflection as control output, few papers use differential propeller thrust.

Because of the low wing loading, slow take-off speed and simple landing gear structure, the unswept flying-wing is easily disturbed by the environment such as the ground-surface undulation and gust wind, and thus the designed on-ground lateral direction controller must have the ability to reject the comprehensive disturbances. Han[10] and Gao[11] proposed active disturbance rejection control (ADRC) technique by improving the proportional integral derivative (PID) control method, in which the extended state observer (ESO) is adopted to estimate and reject the disturbances. Different from other modern control theories, ADRC is similar to PID which does not require accurate mathematical model of the controlled object. This makes the ADRC competent in practical use since the external disturbances cannot be measured in detail. Because of the above characteristics, ADRC is suitable to be used on UAVs which are complex and have large uncertainties. Peng[12, 13] designed the attitude controller based on ADRC for multi-rotor UAV. Wang[14] used ADRC to design the inner loop controllers for small fixed-wing UAVs with modelling uncertainty, the robustness of which was evaluated with simulation and flight experiment. Shao[15] developed the guidance and control systems for missile based on reduced-order ESO. Xia[16] proposed the dynamic model for lateral motion of an autonomous land vehicle and designed a tracking control method based on ADRC and differential flatness. At present, ADRC is mainly used to design the flight attitude controllers for UAVs but there are few researches about on-ground controllers. Meanwhile, most papers stay in the simulation stage without experimental verification.

In this paper, the mathematical model is established for an unswept flying-wing UAV with twin propellers, and a yaw angle controller is designed by using differential propeller thrust based on cascade the ADRC method. Following the yaw angle controller, a straight line trajectory tracker based on improved vector field method is designed. Experimental verifications of the yaw angle controller and trajectory tracker are carried out in order to prove their effectiveness. The control method used in this paper is not only applicable to the unswept flying-wing UAV but also to small utility aircraft using distributed electric propulsion which has become a hot research topic. The structure of landing gear and braking system can be simplified by using this control method.

2.0 MATHEMATICAL MODEL

2.1 Landing gear model

The ground force of the landing gear is shown in Fig. 2. F_n, F_f, F_s denote, respectively, the vertical force, the friction force and the side force. The following assumptions are made in order to simplify the model:

- The pitch and roll angles are very small.
- The side-slip angles of tires are very small.
- The weight and moment of inertia of the tires can be neglected.
- The tires are modelled as damped springs.

The vertical force of each tire is

$$F_{ni} = k_{\delta t}\delta_{ti} + c_{\delta t}\dot{\delta}_{ti}, \quad i = 1, 2, 3, 4 \qquad \ldots(1)$$

https://doi.org/10.1017/aer.2018.167 Published online by Cambridge University Press

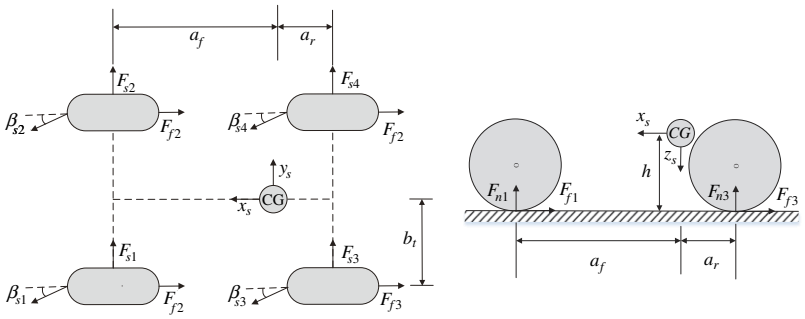


Figure 2. The ground force in top view and left view.

where $k_{\delta t}$ is the equivalent stiffness of tires and $c_{\delta t}$ is the equivalent damping coefficient of tires. δ_{ti} and $\dot{\delta}_{ti}$ are the compression and the compression, respectively, speed of each tire. We can get the compression of each tire by using UAV states and the geometric parameters of landing gear:

$$\begin{cases} \delta_{ti} = \mathrm{sat}(\overline{\delta}_{ti}, 0, \inf), \quad i = 1,2,3,4 \\ \overline{\delta}_{t1} = -H + h - a_f \sin\theta - b_t \sin\phi \\ \overline{\delta}_{t2} = -H + h - a_f \sin\theta + b_t \sin\phi \\ \overline{\delta}_{t3} = -H + h + a_r \sin\theta - b_t \sin\phi \\ \overline{\delta}_{t4} = -H + h + a_r \sin\theta + b_t \sin\phi \end{cases} \quad \ldots(2)$$

where H is the distance from the UAV centre of gravity to ground, while h equals to H when $\delta_{ti} = 0$. b_t is the distance between tires and the symmetric plane of the UAV. a_f and a_r are horizontal distance from front tires and rear tires to the center of gravity. Because the compression of tire cannot be less than 0, the amplitude of the compression must be limited by saturation function and defined as

$$\mathrm{sat}(x, a, b) = \begin{cases} b & x > b \\ x & a < x < b \\ a & x < a \end{cases} \quad \ldots(3)$$

Due to the lack of brake system, the frictional force only contains rolling frictional force which can be expressed as

$$F_{fi} = \mu_f F_{ni}, \quad i = 1,2,3,4 \quad \ldots(4)$$

where μ_f is the frictional coefficient of tires. The study of Zhang[5] shows that when the side-slip angles of tires are very small, the side force can be approximated as

$$F_{si} = k_s \beta_{si} F_{ni}, \quad i = 1,2,3,4 \quad \ldots(5)$$

where k_s and β_s are the cornering stiffness and the slip angle of tires, respectively. As shown in Fig. 2, we can get the side-slip angles:

$$\begin{cases} \beta_{s1} = \arctan\left(-(v + a_f r) / (u + b_t r)\right) \\ \beta_{s2} = \arctan\left(-(v + a_f r) / (u - b_t r)\right) \\ \beta_{s3} = \arctan\left(-(v - a_r r) / (u + b_t r)\right) \\ \beta_{s4} = \arctan\left(-(v - a_r r) / (u - b_t r)\right) \end{cases} \quad \ldots(6)$$

https://doi.org/10.1017/aer.2018.167 Published online by Cambridge University Press

Owing to the fact that the pitch and roll angles are very small, the force and the moment generated by ground are

$$\boldsymbol{F}_{b_t} = \left[-\sum_{i=l}^{4} F_{fi} \quad \sum_{i=1}^{4} F_{si} \quad -\sum_{i=1}^{4} F_{ni} \right]^T \tag{7}$$

$$\boldsymbol{M}_{b_t} = \begin{bmatrix} (F_{n1}-F_{n2}+F_{n3}-F_{n4})b_t - \sum_{i=1}^{4} F_{si}H \\ (F_{n1}+F_{n2})a_f-(F_{n3}+F_{n4})a_r - \sum_{i=1}^{4} F_{fi}H \\ -\left(F_{f1}-F_{f2}+F_{f3}-F_{f4}\right)b_t \end{bmatrix} \tag{8}$$

2.2 Propeller thrust model

A balance is used to measure the thrusts of the propeller in different throttle at zero inflow speed Fig. 3).

When throttle increases from 0 to 1 in every 5 s with a 0.1 step length, the measured thrust is plotted in Fig. 4. Beard[17] proposed a simple model for the thrust generated by a propeller

$$F_p = \frac{1}{2}\rho S_p C_p \left(k_{p1}\delta_p^2 - V_p^2 \right) \tag{9}$$

where S_p, C_p and V_p are the disk area, the thrust coefficient and the inflow speed of the propeller, respectively. When the average of thrust is obtained at every throttle, and the data are fitted with the least square method. It is found that the accuracy of fitting is not high enough and an improvement is proposed as

$$F_p = \frac{1}{2}\rho S_p C_p \left(k_{p1}\delta_p^2 + k_{p2}\delta_p - V_p^2 \right) \tag{10}$$

The data are fitted again with Equation (10). The *R*-square of Equation (9) is 0.917, while the *R*-square of Equation (10) reaches 0.997, showing Equation (10) has a higher fitting precision than Equation (9). The fitting results are shown in Fig. 5.

Without break system, the only way to reduce the aircraft speed is to reverse the propeller. The reverse thrust is shown in Fig. 6. Influenced by the airflow separation of the propeller, the reverse thrust is smaller and contains more noises compared with the forward thrust. The reverse thrust data are fitted with Equations (9) and (10), respectively in Fig. 7. Equation (10) also has a higher fitting precision than Equation (9).

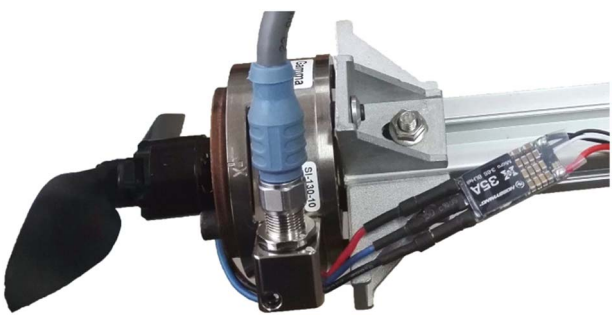


Figure 3. Propeller thrust experiment.

https://doi.org/10.1017/aer.2018.167 Published online by Cambridge University Press

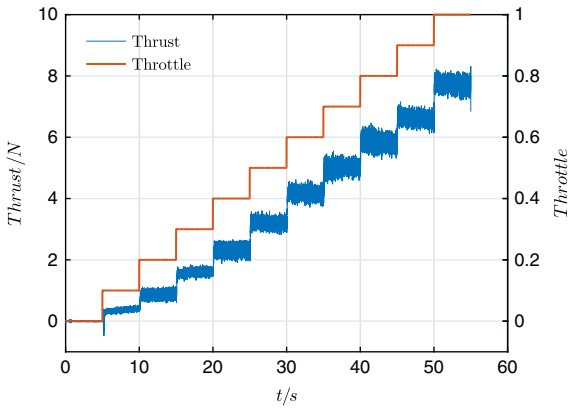


Figure 4. Thrust of the propeller.

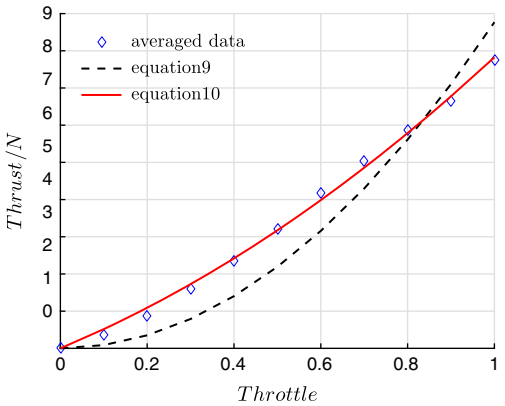


Figure 5. Data fitting of the thrust.

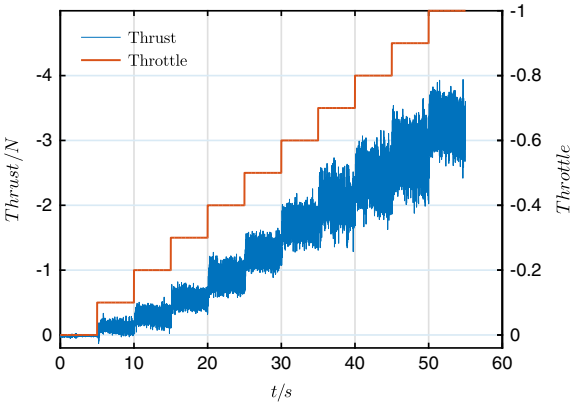


Figure 6. Reverse thrust of the propeller.

https://doi.org/10.1017/aer.2018.167 Published online by Cambridge University Press

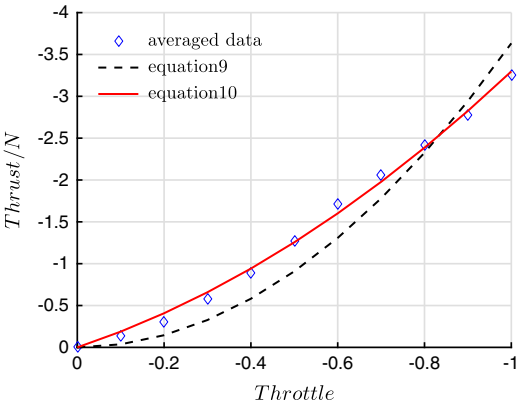


Figure 7. Data fitting of the reverse thrust.

Define $\Delta\delta_p$ as the differential throttle, the throttles of left and right propellers are $\delta_{p_l} = \delta_p + \Delta\delta_p$ and $\delta_{p_r} = \delta_p - \Delta\delta_p$. Meanwhile, the distance between the propellers and the symmetric plane of the UAV is d_p, thus the V_p of left and right propellers are $V_{p_l} = V_a + d_p r$ and $V_{p_r} = V_a - d_p r$. The differential thrust of propeller is

$$\Delta F_p = F_{p_l} - F_{p_r} = \rho S_p C_p (2k_{p1}\delta_p \Delta\delta_p + k_{p2}\Delta\delta_p - 2V_a d_p r)$$

The force and moment generated by propellers are

$$\boldsymbol{F}_{b_p} = [F_{p_l} + F_{p_r} \quad 0 \quad 0]^T \qquad \ldots(11)$$

$$\boldsymbol{M}_{b_p} = [0 \quad 0 \quad \Delta F_p d_p]^T \qquad \ldots(12)$$

2.3 Aerodynamic and gravity model

The aerodynamic forces and moments can be expressed as

$$\begin{cases} F_L = \frac{1}{2}\rho V_a^2 S\left(C_L(\alpha) + C_{L_q}\frac{c}{2Va}q\right) \\ F_Y = \frac{1}{2}\rho V_a^2 S\left(C_Y(\beta) + C_{Y_p}\frac{b}{2Va}p + C_{Y_r}\frac{b}{2Va}r\right) \\ F_D = \frac{1}{2}\rho V_a^2 S\left(C_D(\alpha) + C_{D_q}\frac{c}{2Va}q\right) \end{cases} \qquad \ldots(13)$$

$$\begin{cases} M_l = \frac{1}{2}\rho V_a^2 S\left(C_l(\beta) + C_{l_p}\frac{b}{2Va}p + C_{l_r}\frac{b}{2Va}r\right) \\ M_m = \frac{1}{2}\rho V_a^2 S\left(C_m(\alpha) + C_{m_q}\frac{c}{2Va}q\right) \\ M_n = \frac{1}{2}\rho V_a^2 S\left(C_n(\beta) + C_{n_p}\frac{b}{2Va}p + C_{n_r}\frac{b}{2Va}r\right) \end{cases} \qquad \ldots(14)$$

where C_L, C_Y and C_D are aerodynamic lift, lateral and drag forces coefficients, respectively, of the UAV. C_l, C_m and C_n are aerodynamic roll, pitch and yaw moments coefficients, respectively. V_a, S, b and c are the air-speed, the reference area, the wing span and the mean aerodynamic chord of the aircraft, respectively.

Transform the aerodynamic force and moment from the wind frame to the body frame:

$$\boldsymbol{F}_{b_a} = \mathrm{DCM}_{bw}[-F_D \quad F_Y \quad -F_L]^T \qquad \ldots(15)$$

$$\boldsymbol{M}_{b_a} = [M_l \quad M_m \quad M_n]^T \qquad \ldots(16)$$

https://doi.org/10.1017/aer.2018.167 Published online by Cambridge University Press

Transform the gravity acting on the center of mass to the body frame:

$$\boldsymbol{F}_{b_g} = \mathrm{DCM}_{be}[\,0 \quad 0 \quad mg\,]^T \qquad \ldots(17)$$

2.4 Kinematics and dynamic model

The forces and moments are generated by the ground, propeller propulsion, aerodynamics and gravity

$$\begin{cases} \boldsymbol{F} = \boldsymbol{F}_{b_t} + \boldsymbol{F}_{b_p} + \boldsymbol{F}_{b_a} + \boldsymbol{F}_{b_g} \\ \boldsymbol{M} = \boldsymbol{M}_{b_t} + \boldsymbol{M}_{b_p} + \boldsymbol{M}_{b_a} \end{cases} \qquad \ldots(18)$$

Select the north-east-down positions $\boldsymbol{P} = [\,P_n \quad P_e \quad P_d\,]^T$, body frame velocities $\boldsymbol{V}_b = [\,u \quad v \quad w\,]^T$, Euler angles $\Theta = [\,\phi \quad \theta \quad \psi\,]^T$ and angular rates $\Omega = [\,p \quad q \quad r\,]^T$ as state variables for the UAV, the kinematics and the dynamics of a rigid body can be expressed as

$$\begin{cases} \dot{\boldsymbol{P}} = DCM_{be}^T \boldsymbol{V} \\ \dot{\boldsymbol{V}}_b = -\Omega \times \boldsymbol{V}_b + \boldsymbol{F} / m \\ \dot{\Theta} = \begin{bmatrix} 1 & \sin\phi\tan\theta & \cos\phi\tan\theta \\ 0 & \cos\phi & -\sin\phi \\ 0 & \dfrac{\sin\phi}{\cos\theta} & \dfrac{\cos\phi}{\cos\theta} \end{bmatrix} \Omega \\ \dot{\Omega} = J^{-1}(-\Omega \times (J\Omega) + \boldsymbol{M}) \end{cases} \qquad \ldots(19)$$

3.0 ON-GROUND LATERAL DIRECTION CONTROL LAW DESIGN

The purpose of on-ground lateral direction control law is to control the movement of UAVs along the yaw angle command or tracking a trajectory. So the control law is composed of a yaw controller and a straight line trajectory tracking controller.

3.1 Yaw controller design based on ADRC

In order to design the controller more conveniently, only the yaw angle and the yaw angle rate are taken into consideration, Equation (19) can be simplified as

$$\begin{cases} \dot{\psi} = \dfrac{\sin\phi}{\cos\theta} q + \dfrac{\cos\phi}{\cos\theta} r \\ \dot{r} = \dfrac{\left[J_{xx}(J_{xx} - J_{yy}) + J_{xz}^2\right] pq - J_{xz}(J_{xx} - J_{yy} + J_{zz}) qr}{J_{xx}J_{zz} - J_{xz}^2} + \dfrac{[\,J_{xz} \quad 0 \quad J_{xx}\,]\boldsymbol{M}}{J_{xx}J_{zz} - J_{xz}^2} \end{cases} \qquad \ldots(20)$$

Equation (20) can be considered as two first-order systems in series. According to the time scale separation theory, the yaw angle control loop and yaw angle rate control loop can be designed separately. So the controller is designed on the base of cascade ADRC theory, and the controller structure is shown in Fig. 8

https://doi.org/10.1017/aer.2018.167 Published online by Cambridge University Press

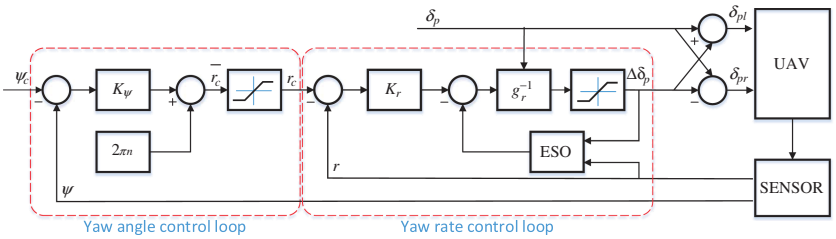


Figure 8. Yaw controller structure.

3.1.1 Yaw angle control loop

Owing to the fact that the pitch and roll angles are quite small, the first item of equation (20) can be further simplified as

$$\dot{\psi} = r \qquad \ldots(21)$$

Since Equation (21) is homogeneous, it's not necessary to design an ESO for yaw angle control loop. This can not only reduce the amount of computation but also avoid the influence of yaw angle singularity to ESO.

The feedback control law of yaw angular is designed as follows:

$$\begin{cases} \bar{r}_c = K_\psi(\psi_c - \psi + 2\pi n) \\ r_c = \mathrm{sat}(\bar{r}_c, -r_{c\max}, r_{c\max}) \end{cases} \qquad \ldots(22)$$

The maximum yaw angle rate of UAV is finite, therefore, use $r_{c\max}$ to limit the maximum value of yaw angle command. Because there is a singularity in yaw angle, it is necessary to select the appropriate integer n in order to make the error of yaw angle command and yaw angle within the reasonable range:

$$-\pi < \psi_c - \psi + 2\pi n < \pi \qquad \ldots(23)$$

3.1.2 Yaw angle rate control loop

The second item of Equation (20) can be expressed as

$$\dot{r} = f_r + g_r \Delta\delta_p \qquad \ldots(24)$$

f_r is denoted as the total disturbance. Because of the disturbance on the ground run, f_r is a multi-variable function of both the states and external disturbances. In practice, f_r is complicated and unmeasurable.

g_r is the control efficiency of $\Delta\delta_p$ where

$$g_r = \frac{J_{xx}}{J_{xx}J_{zz} - J_{xz}^2}\left(\rho S_p C_p(2k_{p1}\delta_p + k_{p2})\right)d_p$$

as shown in Figs 5 and 7, k_{p1} and k_{p2} have different values when the throttle is greater or less than zero, and, thus, g_r will change rapidly when the UAV starts using reverse thrust of propeller to slow down. The sharp change of g_r demands a faster response and better robustness of the controller.

https://doi.org/10.1017/aer.2018.167 Published online by Cambridge University Press

The ESO is the key to ADRC, which is able to observe the total disturbance in real time and will be feedback to the control law:

$$\begin{cases} e_r = \hat{r} - r \\ \dot{\hat{r}} = \hat{\Delta}_r - \beta_{01} e_r + g_r \Delta\delta_p \\ \dot{\hat{\Delta}}_r = -\beta_{02} \mathrm{fal}(e, \sigma, \delta) \end{cases} \quad \ldots(25)$$

where $\hat{\Delta}_r$ is the estimated value of f_r. e_r is the observer error. β_{01} and β_{02} are observer gains. Function fal(e, σ, δ) is defined as[10]

$$\mathrm{fal}(e, \sigma, \delta) = \begin{cases} \dfrac{e}{\delta^{1-\sigma}}, & |e| \le \delta \\ |e|^{\sigma} \operatorname{sign}(e), & |e| > \delta \end{cases} \quad \ldots(26)$$

where sign(·) is the signum function.

The feedback control law of yaw angular rate is designed as

$$\begin{cases} \overline{\Delta}\delta_p = \left(K_r (r_c - r) - \hat{\Delta}_r\right) g_r^{-1} \\ \Delta\delta_p = \mathrm{sat}(\overline{\Delta}\delta_p, -\Delta\delta_{p\max}, \Delta\delta_{p\max}) \end{cases} \quad \ldots(27)$$

To reduce the effect of differential propeller thrust on total thrust, it is necessary to limit the amplitude of differential propeller thrust. $\Delta\delta_{p\max}$ is the maximum allowable value of $\Delta\delta_p$ while $-\Delta\delta_{p\max}$ is the minimum value. It is worth noting that Equation (25) must use $\Delta\delta_p$ as an input rather than $\overline{\Delta}\delta_p$ in order to avoid ESO saturation. This is more intuitive and effective than the integral saturation limitation of the PID controller.

3.2 Straight line trajectory tracking controller design based on vector field

Assuming that the error between the yaw angle and the speed yaw angle can be ignored, the distance between UAV and the straight line path is

$$\dot{d} = V \sin(\psi - \psi_t)$$

Nelson[18] proposed a path following method based on vector field and gave the proof of stability, and the designed yaw angle command of UAV is given in Equation (28). Sujit[19] compared the vector field (VF) path-following control law with non-linear guidance law,

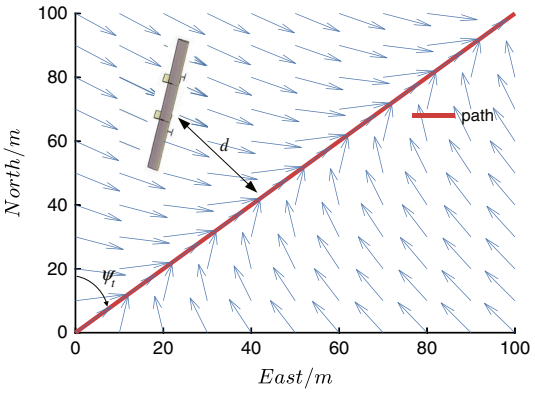


Figure 9. Vector field path following.

https://doi.org/10.1017/aer.2018.167 Published online by Cambridge University Press

vector-field has lower cross-track error. The illustration of the vector-field path-following control is shown in Fig. 9:

$$\psi_c = \psi_t - \psi^{\infty}\frac{2}{\pi}\tan^{-1}(K_d d) + 2\pi l \quad \ldots(28)$$

where d is the lateral distance of the UAV from the straight line path, ψ_t is the direction angle of the straight line path, $\psi^{\infty} \in \left(0, \frac{\pi}{2}\right]$ is the maximum value of the angle between ψ_c and ψ_t and l is an integer which makes yaw angle command within the reasonable range.

It is obvious that Equation (28) is designed for the condition of constant velocity; however, during ground control, the velocity has a wide range of variation. The parameter K_d is redefined to increase the applicability of Equation (28) in practice

$$K_d = \overline{K}_d \,/\, \mathrm{sat}(V, V_{\min}, \inf) \quad \ldots(29)$$

where $V_{\min}$ is the lowest speed range to avoid singularity.



Figure 10. Experimental aircraft.

Table 1
The main specifications of the UAV in this paper

Specifications	Wing-span	Mean aero-dynamic chord	Weight	Motor	Battery
Value	1.80 m	0.18 m	1.5 kg	Sunny sky 2216	3 s 3400 mAh

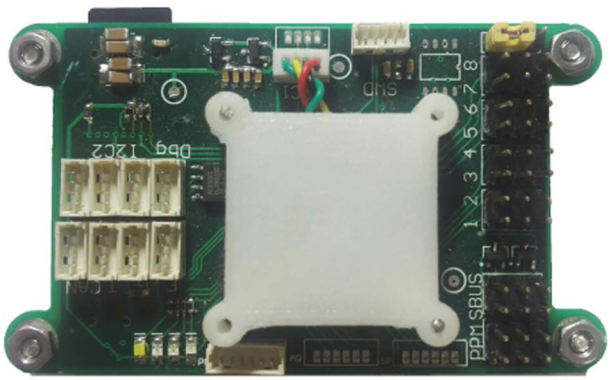


Figure 11. Autopilot.

https://doi.org/10.1017/aer.2018.167 Published online by Cambridge University Press

Table 2
Autopilot hardware

Hardware	Processor	Gyro accelerator	Compass	Air pressure	Air speed	GPS
Type	Stm32f407	Mpu6050	Hmc5883l	Ms5611	Ms4525do	Ublox m8n

4.0 EXPERIMENT AND RESULTS

4.1 Hardware testbed

Figure10 shows the UAV used for the ground run tests reported in this paper. The aircraft is made by 3D-printer. The main specifications of this UAV are given in Table 1.

Figure 11 shows the autopilot used in the tests, which is equipped with an arm-cortex-m4 processor, rate gyro, accelerator, magnetic compass and air pressure sensor. Meanwhile, the autopilot is also connected with global positioning system (GPS), air speed sensor, 900MHz radio modem, SBUS/IBUS remote control receiver, electrical motor speed controllers (ESC) and digital servos on the aircraft. The hardware parameters are shown in Table 2.

4.2 Experimental results

To verify the effectiveness, robustness and performance of the proposed ADRC yaw angle controller and the VF straight line trajectory tracking controller for on-ground lateral direction control, experiments have been carried out on the unswept flying-wing UAV, which is introduced in the previous section. At the same time, the PID yaw angle controller with the same gain parameters as the designed yaw angle controller is used for the contrast experiment. The parameter values of the control law used in the experiment are given in Table 3.

4.2.1 Experimental results of yaw controller

The performance and robustness of the controller is analysed in three experiments:

(A) Tracking step signal input command

In this experiment, the input command ψ_c is set as step signal with 90° amplitude. The throttle is fixed on 0.3. Figure 12 shows the response comparison between ADRC yaw controller and PID yaw controller.

Figure 12(a) shows that the ADRC yaw angle controller is able to track the input command smoothly and without overshoot. The rise time of ADRC controller is 4.6 s when tracking 90° command, which is smaller than PID controller's 5.1 s. Meanwhile, the average tracking error from 8 to 10 s of ADRC is 2.34° while that of PID controller is 3.13°; therefore, ADRC yaw angle controller has a better control precision. As shown in Fig. 12(b), yaw rate can reach

Table 3
Parametres of controllers

	β_{01}	β_{02}	σ	δ	K_r	$\Delta\delta_{pmax}$	K_ψ	r_{cmax}	ψ^∞	$\overline{K}_d$	V_{min}
Value	300	400	0.5	0.1	10	0.15	1	π/6	π/2	0.2	1
Equation	(25)	(25)	(25)	(25)	(27)	(27)	(22)	(22)	(28)	(29)	(29)

https://doi.org/10.1017/aer.2018.167 Published online by Cambridge University Press

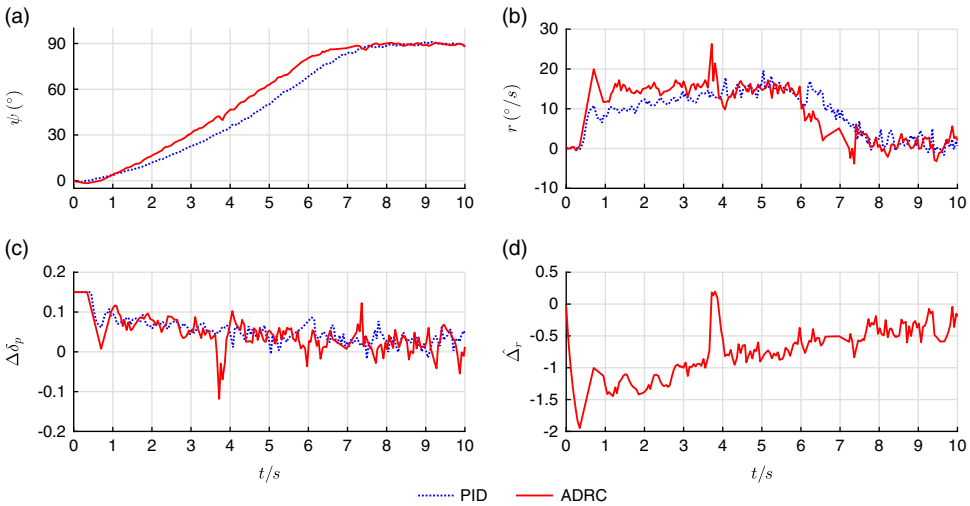


Figure 12. The response curves of the ADRC and PID yaw controllers when tracking step command.

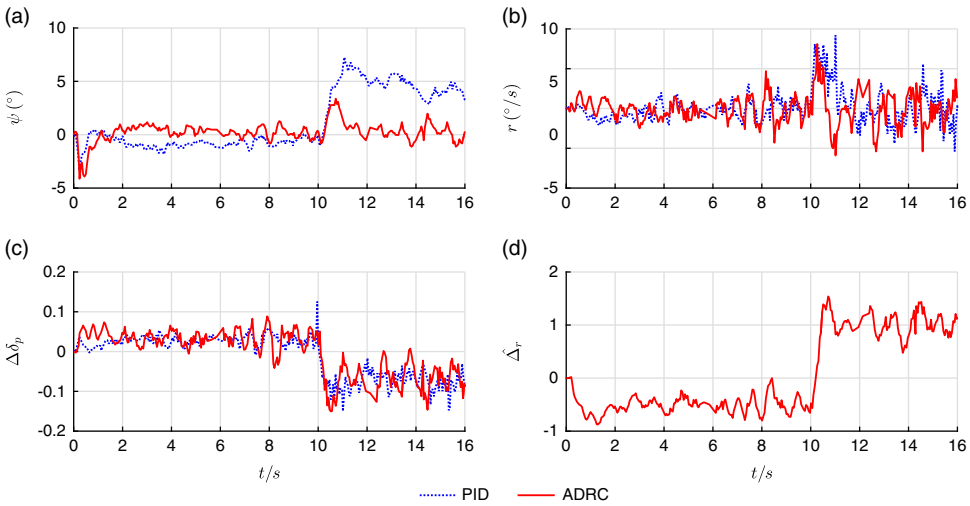


Figure 13. The response curves of the ADRC and PID yaw controllers after being disturbed.

$r_{\text{cmax}} = 15°/\text{s}$ within 1 s by using ADRC controller, in stand of 4 s by using PID controller. Figure 12(c) shows that the control output jitter of ADRC controller is bigger than that of PID controller because of ESO observing the ground undulation.

(B) Response to disturbance

In the process of ground control, there will be many external disturbances. In order to make the experiment more representative, a 0.1 differential propeller thrust is artificially added in the experiment at 10 s. The input command and throttle are fixed on 0 and 0.3 respectively. Figure 13 shows the response results of ADRC and PID yaw controllers.

Figure 13(a) shows that after being disturbed, the ADRC controller can converge quickly and the influence of disturbance is much smaller than that of PID controller, because Fig. 13

https://doi.org/10.1017/aer.2018.167 Published online by Cambridge University Press

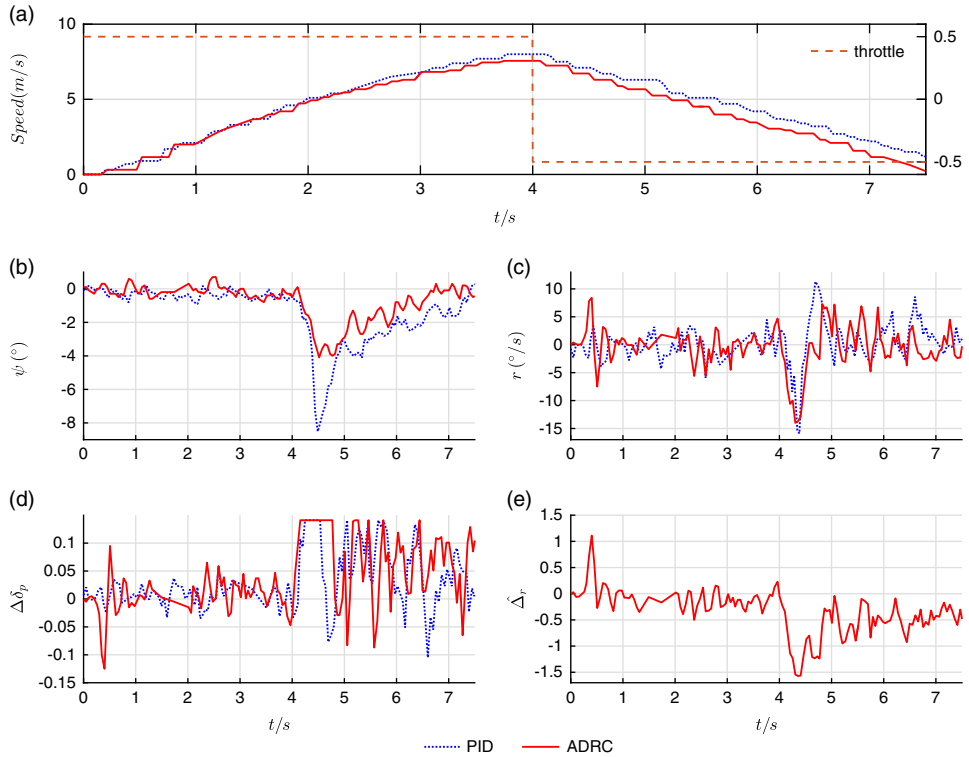


Figure 14. The response curves of the ADRC and PID yaw controllers during the process of reducing speed.

(d) shows that the ESO observes the disturbance immediately. It can be seen that the ADRC yaw controller has a better robustness than the PID yaw controller.

(C) Response to controller switching

An experiment is designed to test the yaw controller efficiency when the UAV is reducing speed. During the first 4 s of the experiment, 0.5 throttle is used to accelerate the speed, then −0.5 throttle is used to decelerate. Because the rotating speed of the propeller varies greatly, there is a strong non-linearity in thrust and reverse thrust switching. In the process of switching, the controllability of the aircraft is very weak. Figure 14 shows the responses of ADRC and PID yaw controllers.

Figure 14(a) shows the speed of UAV measured by GPS. As shown in Fig. 14(b), because of the incomplete symmetry of UAV, the UAV turns left at the beginning of the switching. Meanwhile, in Fig. 14(c), the ADRC controller outputs the maximum differential propeller thrust immediately while the PID controller is obviously much slower. Figure 14(b) shows that due to better robustness and faster response speed, the maximum tracking error of ADRC yaw controller is half of that of the PID controller.

4.2.2 Vector field straight line trajectory tracking controller

Figure 15 shows the experimental results of trajectory tracking controllers which uses ADRC and PID controllers as inner loop when tracking 3m step command.

Figure 15(a) shows that vector field trajectory tracking controller is able to track the straight line, and, at the same time, when ADRC is used as the inner loop controller, it has

https://doi.org/10.1017/aer.2018.167 Published online by Cambridge University Press

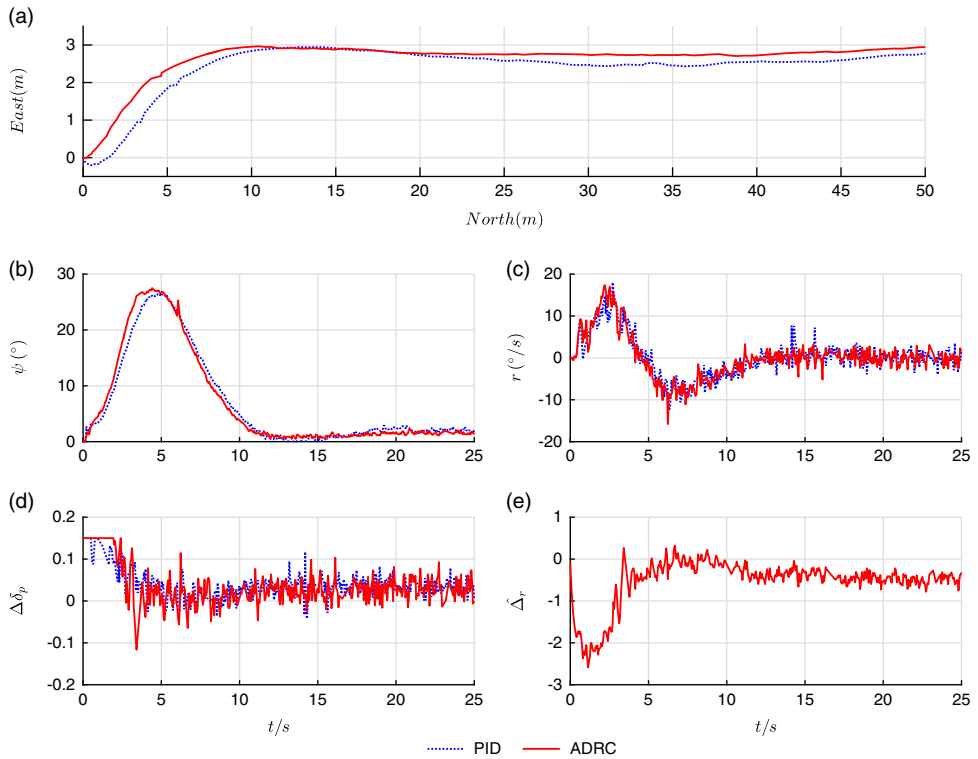


Figure 15. The response curves of straight line trajectory tracking controllers.

better rate of convergence and control accuracy than the PID controller. Because of the small error between the yaw angle measured by attitude and heading reference system (AHRS) and the actual yaw angle, a static-state error exists in the experiment. But considering the accuracy of GPS, this static-state error is in an acceptable range.

5.0 CONCLUSIONS

This paper presents the modelling, autopilot control law design and experiment tests on how to control the lateral direction of the unswept flying-wing UAV when it is moving on-ground by using differential propeller thrust instead of rudder control surface and front wheel steering system as the control outputs. The differential propeller thrust can be used not only in common ground moving but also in speed reducing by the reverse propeller thrust instead of breaking system.

The on-ground lateral direction controller consists of a yaw angle control law on the basis of ADRC and straight line trajectory tracking based on improved vector field method. The experiment results show that the designed control law has high control efficiency, response speed and robustness.

REFERENCES

1. FLITTIE, K. and CURTIN, B. Pathfinder solar-powered aircraft flight performance, American Institute of Aeronautics and Astronautics Conference, AIAA, August 1998, Boston, MA, USA, pp 618–632.

https://doi.org/10.1017/aer.2018.167 Published online by Cambridge University Press

2. COLELLA, N.J. and WENNEKER, G.S. Pathfinder. Developing a solar rechargeable aircraft, *IEEE Potentials*, 1996, **15**, (1), pp 18–23.
3. NOLL, T.E., BROWN, J.M. and PEREZ-DAVIS, M.E. Investigation of the Helios Prototype Aircraft Mishap Volume I Mishap Report, *NASA*, 2004.
4. EHERNBERGER, L.J., DONOHUE, C. and TEETS, E.H. A review of solar-powered aircraft flight activity at the Pacific missile range test facility, Kauai, Hawaii, *Extended Abstracts*, 2004.
5. ZHANG, Y. and DUAN, H. A directional control system for UCAV automatic takeoff roll, *Aircr Engineering & Aerospace Technology*, 2013, **85**, (1), pp 48–61.
6. LEMAY, D., CHAMAILLARD, Y. and BASSET, M. Gain-scheduled yaw control for aircraft ground taxiing, *IFAC Proceedings Volumes*, 2011, **44**, (1), pp 12970–12975.
7. CHEN, B.H., JIAO, Z.X. and SHUZHI, S.G. Aircraft-on-ground path following control by dynamical adaptive backstepping, *Chinese J Aeronautics* , 2013, **26**, (3), pp 668–675.
8. RE, F. Modelica landing gear modelling and on-ground trajectory tracking with sliding mode control, 1st CEAS Specialist Conference on Guidance, Navigation and Control, AIAA & CEAS, April 2011, pp 103–115.
9. BIANNIC, J., MARCOS, A. and JEANNEAU, M. Nonlinear simplified LFT modelling of an aircraft on ground, 2006 IEEE International Conference on Control Application, 2006, pp 2213–2218.
10. HAN, J. From PID to active disturbance rejection control, *IEEE Transactions on Industrial Electronics*, 2009, **56**, (3), pp 900–906.
11. GAO, Z. Active disturbance rejection control: a paradigm shift in feedback control system design, American Control Conference, IEEE, June 1998, pp 2399–2405.
12. PENG, C., TIAN, Y.T. and GONG, X. ADRC trajectory tracking control based on PSO algorithm for a quad-rotor, IEEE Conference on Industrial Electronics and Applications, IEEE, June 2013, pp 800–805.
13. FU, C., TIAN, Y.T. and PENG, C. Path tracking control for eight-rotor aircraft based on linear ADRC algorithm, IEEE Conference on Industrial Electronics and Applications, IEEE, June 2016, pp 2147–2152.
14. WANG, X., KONG, W. and ZHANG, D. Active disturbance rejection controller for small fixed-wing UAVs with model uncertainty, IEEE International Conference on Information and Automation, 2015, pp 2299–2304.
15. XINGLING, S. and HONGLUN, W. Back-stepping active disturbance rejection control design for integrated missile guidance and control system via reduced-order ESO, *Isa Transactions*, 2015, **57**, (4), pp 10–22.
16. XIA, Y., PU, F. and LI, S. Lateral path tracking control of autonomous land vehicle based on ADRC and differential flatness, *IEEE Transactions on Industrial Electronics*, 2016, **63**, (5), pp 3091–3099.
17. BEARD, R.W. and MCLAIN, T.W. *Small Unmanned Aircraft: Theory and Practice*, 2012, Princeton University Press, New Jersey, US.
18. NELSON, D.R., BARBER, D.B. and MCLAIN, T.W. Vector field path following for miniature air vehicles, *IEEE Transactions on Robotics*, 2007, **23**, (3), pp 519–529.
19. SUJIT, P., SARIPALLI, S. and SOUSA, J.B. Unmanned aerial vehicle path following: a survey and analysis of algorithms for fixed-wing unmanned aerial vehicles, *IEEE Control Systems*, 2014, **34**, (1), pp 42–59.

https://doi.org/10.1017/aer.2018.167 Published online by Cambridge University Press